

Crustal layering in northeastern Tibet: a case study based on joint inversion of receiver functions and surface wave dispersion

Yangfan Deng,^{1,2} Weisen Shen,³ Tao Xu^{2,4} and Michael H. Ritzwoller³

¹State Key Laboratory of Isotope Geochemistry, Guangzhou Institute of Geochemistry, Chinese Academy of Sciences, Guangzhou, 510640, China

²State Key Laboratory of Lithospheric Evolution, Institute of Geology and Geophysics, Chinese Academy of Sciences, Beijing, 100029, China

³Department of Physics, University of Colorado at Boulder, Boulder, CO 80309, USA. E-mail: Weisen.Shen@colorado.edu

⁴CAS Center for Excellence in Tibetan Plateau Earth Sciences, Beijing, 100101, China

Accepted 2015 July 28. Received 2015 July 27; in original form 2015 March 23

SUMMARY

Recently constructed models of crustal structure across Tibet based on surface wave data display a prominent mid-crustal low velocity zone (LVZ) but are vertically smooth in the crust. Using six months of broad-band seismic data recorded at 22 stations arrayed approximately linearly over a 440 km observation profile across northeastern Tibet (from the Songpan–Ganzi block, through the Qaidam block, into the Qilian block), we perform a Bayesian Monte Carlo joint inversion of receiver function data with surface wave dispersion to address whether crustal layering is needed to fit both data sets simultaneously. On some intervals a vertically smooth crust is consistent with both data sets, but across most of the observation profile two types of layering are required: a discrete LVZ or high velocity zone (HVZ) formed by two discontinuities in the middle crust and a doublet Moho formed by two discontinuities from 45–50 km to 60–65 km depth connected by a linear velocity gradient in the lowermost crust. The final model possesses (1) a mid-crustal LVZ that extends from the Songpan–Ganzi block through the Kunlun suture into the Qaidam block consistent with partial melt and ductile flow and (2) a mid-crustal HVZ bracketing the south Qilian suture coincident with ultrahigh pressure metamorphic rocks at the surface. (3) Additionally, the model possesses a doublet Moho extending from the Qaidam to the Qilian blocks which probably reflects increased mafic content with depth in the lowermost crust perhaps caused by a vertical gradient of eclogitization. (4) Crustal thickness is consistent with a step-Moho that jumps discontinuously by 6 km from 63.8 km (± 1.8 km) south of 35° to 57.8 km (± 1.4 km) north of this point coincident with the northern terminus of the mid-crustal LVZ. These results are presented as a guide to future joint inversions across a much larger region of Tibet.

Key words: Tomography; Surface waves and free oscillations; Continental margins: convergent; Crustal structure.

1 INTRODUCTION

The expansion of seismic instrumentation in Tibet has led to the rapid emergence of velocity models of the Tibetan crust and upper mantle. The emplacement of broad-band seismometers, in particular, allows for the observation of surface waves based both on ambient noise (e.g. Yao *et al.* 2006; Yang *et al.* 2010; Zheng *et al.* 2010; Zhou *et al.* 2012; Karplus *et al.* 2013) and earthquake data (e.g. Caldwell *et al.* 2009; Feng *et al.* 2011; Li *et al.* 2013a,b; Zhang *et al.* 2014). Studies based on surface waves provide information primarily about shear wave speeds in the crust and uppermost mantle beneath Tibet (e.g. Villasenor *et al.* 2001; Yao *et al.* 2008; Li *et al.* 2009; Duret *et al.* 2010; Huang *et al.* 2010; Guo *et al.* 2012; Yang *et al.* 2012; Li *et al.* 2013b; Xie *et al.* 2013; Chen *et al.* 2014).

A positive attribute of surface wave studies is that information is spread homogeneously across much of Tibet, but at the price of relatively low resolution both laterally and vertically. The vertical resolution of models derived from surface waves presents a particular challenge, as surface waves do not image discontinuities in seismic velocities well. Receiver functions image internal interfaces better than surface waves and there have been several studies based on them across Tibet (e.g. Zhu & Helmberger 1998; Vergne *et al.* 2002; Wittlinger *et al.* 2004; Xu *et al.* 2007; Shi *et al.* 2009; Zhao *et al.* 2011; Sun *et al.* 2012; Yue *et al.* 2012; Tian & Zhang 2013; Xu *et al.* 2013b; Tian *et al.* 2014; Zhang *et al.* 2014). Receiver functions, however, only provide information near seismic stations and less powerfully constrain structures between interfaces than surface waves (e.g. Ammon *et al.* 1990). The joint interpretation of receiver

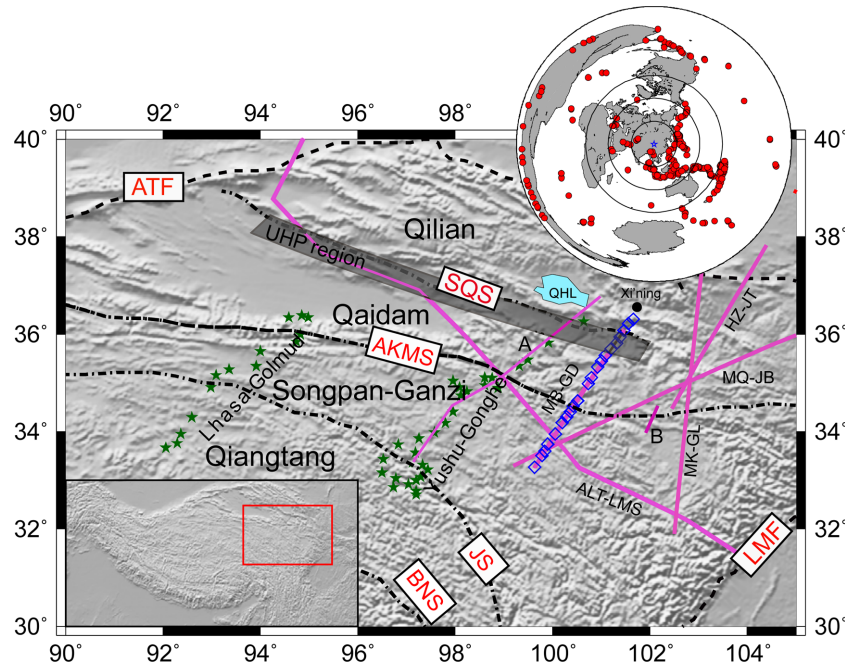


Figure 1. The inset map presents locations of the distribution of teleseismic earthquakes used in this study. Blue diamonds are the locations broad-band seismometers used in this study; green stars are earlier seismic stations from the Lhasa-Golmud and Yushu-Gonghe profiles. Deep seismic sounding profiles and seismic reflection profiles include the following: HZ-JT: Hezuo–Jingtai profile (Zhang *et al.* 2013); MB-GD: Moba–Guide profile (Zhang *et al.* 2011a); ALT-LMS: Altyn Tagh–Longmenshan profile (Wang *et al.* 2013); MK-GL: Markang–Gulang profile (Zhang *et al.* 2008); MQ-JB: Maqin–Jingbian profile (Liu *et al.* 2006); A: Galvé *et al.* (2002); B: Wang *et al.* (2011). Geological features include: ATF: Altyn Tagh fault; BNS: Bangong–Nujiang suture; LMF: Longmenshan fault; JS: Jinsha suture, AKMS: Animaqing–Kunlun–Muztagh suture (or Kunlun fault), SQS: south Qilian suture and the Songpan–Ganzi, Qaidam block and Qilian blocks are identified. The region with ultrahigh pressure (UHP) metamorphism is identified by the grey rectangle (Yang *et al.* 2002).

functions along with surface wave dispersion, however, provides information about vertical layering that surface waves alone may miss (e.g. Ozalabey *et al.* 1997; Julia *et al.* 2000; Bodin *et al.* 2012; Shen *et al.* 2013a). Using data from the USArray in the US, Shen *et al.* (2013a) present a method to invert receiver functions and surface wave dispersion jointly based on a Bayesian Monte Carlo method to produce a model of shear wave speeds (and other variables) along with uncertainties in the crust and uppermost mantle. Shen *et al.* (2013b,c) show that vertically smooth crustal models can fit both data sets acceptably except in several regions and, therefore, across most of the western and central US the introduction of layering within the crystalline crust is not required to fit the receiver function data used in their study.

The purpose of this paper is to address the same questions for Tibet with a particular focus on northeastern Tibet: (1) Can surface wave dispersion and receiver function data be fit simultaneously with vertically smooth models in the crystalline crust? (2) If not, then what is the nature of the discontinuities between the sediments and Moho that must be introduced to allow both data sets to be fit simultaneously? (3) Finally, what do the answers to these questions imply about the thickness and structure of the crust in northeastern Tibet?

In this study we use six months of data (late 2010 to mid-2011) from a linear array of 22 broad-band seismometers deployed in the Songpan–Ganzi block, the Qaidam block and the Qilian block of northeastern Tibet (Fig. 1, blue diamonds). We use these data to produce receiver functions (with uncertainties) at 23 evenly spaced geographical locations spanning a distance of 440 km along the ‘observation profile’. Using the method of Shen *et al.* (2013a), we jointly invert these receiver functions along with Rayleigh wave

phase speed data taken from the study of Xie *et al.* (2013) to produce shear velocity models (with uncertainties) of the crust and uppermost mantle beneath the observation profile. We produce two models, one that varies smoothly vertically in the crystalline crust (Model 1) and another one (Model 2) that allows for crustal discontinuities that are adapted to the receiver functions. In contrast to the US (Shen *et al.* 2013b,c), we present evidence here that across most of the observation profile crystalline crustal discontinuities and/or a doublet Moho are needed to fit the receiver functions.

The crust in northeastern Tibet has already been the subject of studies based on seismic reflection and refraction profiling (see Fig. 1) as well as receiver functions (e.g. Vergne *et al.* 2002; Shi *et al.* 2009; Zhao *et al.* 2011; Yue *et al.* 2012; Tian & Zhang 2013; Xu *et al.* 2013b; Tian *et al.* 2014). These studies have observed significant variations in crustal structure (e.g. Karplus *et al.* 2011; Mechie *et al.* 2012) and thickness, including in some cases stepwise thickening of Moho (e.g. Zhu & Helmberger 1998; Vergne *et al.* 2002; Wittlinger *et al.* 2004; Jiang *et al.* 2006). Understanding such variations is critical to test conflicting hypotheses related to the formation and evolution of the Tibetan plateau (e.g. Molnar *et al.* 1993; Tapponnier *et al.* 2001). Northeastern Tibet also is the site of choice to study remote effects of the India–Asia collision (Metivier *et al.* 1998; Meyer *et al.* 1998; Chen *et al.* 1999; Pares *et al.* 2003). In addition, the region contains the Caledonian orogeny and petrological and isotopic data point to high pressure and ultrahigh pressure (UH/UHP) metamorphism (Liu *et al.* 2003; Luo *et al.* 2012), which is inferred from the presence of eclogite and garnet peridotite as well as coesite-bearing gneiss in the north Qaidam (Song 1996; Yang *et al.* 2002; Song *et al.* 2006). Such metamorphism may have

been caused by the burial and exhumation of the metamorphic rocks in the uppermost mantle along a Palaeozoic subduction zone (e.g. Yin *et al.* 2007).

We are, nevertheless, unaware of previous studies based on the joint inversion of surface wave data and receiver function across northeastern Tibet. Other researchers have performed such joint inversions elsewhere in Tibet, notably in southeast Tibet or southwest China (e.g. Li *et al.* 2008; Sun *et al.* 2014; Wang *et al.* 2014; Bao *et al.* 2015) and the Lhasa terrane (e.g. Xu *et al.* 2013a). Thus, the models produced in this study both may guide future joint inversions at large scales across Tibet and also provide new information about the structure and thickness of the crust in northeastern Tibet.

In Section 2, we discuss the receiver function and surface wave phase speed data sets that we use in the joint inversion. The hypothesis test to determine if crystalline crustal layering is needed and its characteristics are presented in Section 3, in which we contrast model characteristics and data fit with and without intra-crustal layering. In Section 4, we discuss the implications of the final crustal velocity model (Model 2) in terms of mid-crustal partial melt in the Songpan–Ganzi block and its potential intrusion into the Qaidam block, the coincidence of a mid-crustal high velocity zone (HVZ) with HP/UHP rocks in the Qaidam block, the nature and location of the Moho doublets and the step-Moho along the observation profile, and finally compare our estimates of crustal thickness with earlier studies in the region.

2 DATA AND METHODOLOGY

Between November 2010 and June 2011, a passive seismic experiment was carried out by the Institute of Geology and Geophysics, Chinese Academy of Sciences, from the Songpan–Ganzi block to the Qilian block (Fig. 1). Twenty-two broad-band seismographs (Reftek-72A data loggers and Guralp CMG3-ESP sensors with 50 Hz–30 s bandwidth; represented by the blue diamonds in Fig. 1) were deployed at intervals of about 20 km. The profile covers the northeastern margin of the Tibetan plateau. The northwest–southeast trending Animaqing–Kunlun–Muztagh suture (Kunlun fault) and the south Qilian suture divide the profile into three principal geological units: the Songpan–Ganzi block, the Qaidam block and the Qilian block.

2.1 Receiver functions

2.1.1 Sensor orientation

Misorientation of sensors will cause amplitude errors in receiver functions (Niu & Li 2011). Before computing the receiver functions, we attempt to determine station orientation using *P*-wave particle motions (e.g. Niu & Li 2011). A misorientation less than 7° in azimuth is not expected to affect receiver functions or surface wave polarizations significantly (Niu & Li 2011). We found that only one of the 22 stations exhibited a misorientation azimuth larger than 7°, and corrected the orientation for this station.

2.1.2 Calculation of receiver functions

Receiver functions are determined by deconvolving the vertical component seismogram from the radial component, thereby isolating the receiver site effects from other information contained in

the teleseismic *P* waveforms (e.g. Ammon 1991). We write this schematically in the frequency (ω) domain as follows:

$$\text{RF}(\omega) = \frac{R(\omega)}{V(\omega)} \quad (1)$$

where $R(\omega)$ is the radial component at a particular station, $V(\omega)$ is the vertical component and $\text{RF}(\omega)$ is the receiver function which is typically displayed after it is transformed back into the time domain to produce $\text{RF}(t)$. In practice, however, after rotating the observed north and east components to the radial and transverse directions, we calculate the receiver functions using a time-domain iterative deconvolution method (Ligorria & Ammon 1999). This process utilizes an interactive linear inversion algorithm to perform the deconvolution in the time domain with the assumption that the resulting receiver function is a sum of Gaussian pulses. In theory, the convolution of the resulting receiver function with the vertical would reproduce the radial component. However, the assumption we used in the deconvolution process prohibits the recovery to be perfect, and we can further use the recovery rate to identify bad receiver functions, which will be discussed in Section 2.1.3. During the deconvolution, we apply a low-pass Gaussian filter to produce receiver functions with a dominant period of about 1 s, thereby reducing high-frequency noise (and signal). Prior to this calculation, we selected teleseismic *P* waveforms from earthquakes with magnitudes $M_w \geq 5.5$ in the epicentral distance range from 30° to 90° (Fig. 1, inset). We make corrections to the receiver functions in both time and amplitude by normalizing to a reference slowness of 0.06 deg s⁻¹ (Jones & Phinney 1998). Those receiver functions that have *P* wave slownesses greater than 0.1 deg s⁻¹ or smaller than 0.04 deg s⁻¹ are discarded before the normalization. The V_p/V_s ratio is set to 1.75 in both the crust and mantle. The reason for this choice and its effects are discussed later in the paper.

2.1.3 Quality control

Following Shen *et al.* (2013a), we perform a three-step quality control process. Step 1: We remove receiver functions whose product with the vertical component seismogram poorly approximates the radial component (<80 per cent recovery rate of the observed power in the radial seismogram). Step 2: We remove receiver functions with unrealistic amplitudes at zero time (greater than 1 or smaller than 0.02). Step 3: We employ a method known as ‘harmonic stripping’ (Shen *et al.* 2013a) to remove receiver functions that do not vary smoothly in azimuth. If j denotes the earthquake index, an observed receiver function at a particular station derives from a *P* wave that propagates at azimuth θ_j and is denoted $\text{RF}(\theta_j, t)$. In this step, we fit a truncated harmonic function to all such observed receiver functions from different earthquakes (i.e. azimuths) for each station at each time t as follows:

$$H(\theta, t) = A_0(t) + A_1(t) \sin[\theta + \alpha_1(t)] + A_2(t) \sin[2\theta + \alpha_2(t)]. \quad (2)$$

Here, the time functions A_i ($i = 0, 1, 2$) are the amplitudes of the three harmonic components of the receiver functions and the angles α_i are the initial phases for the azimuthally dependent components. This harmonic analysis is designed to identify the azimuthally smooth structural effects. For a given earthquake j , we define the difference function $D(j)$ as the root mean square (rms) of the difference between the observed receiver function for this earthquake, $\text{RF}(\theta_j, t)$ and the harmonic fit $H(\theta, t)$ when $\theta_j = \theta$:

$$D(j) = \sqrt{\frac{1}{t_f - t_i} \int_{t_i}^{t_f} (\text{RF}(\theta_j, t) - H(\theta_j, t))^2 dt} \quad (3)$$

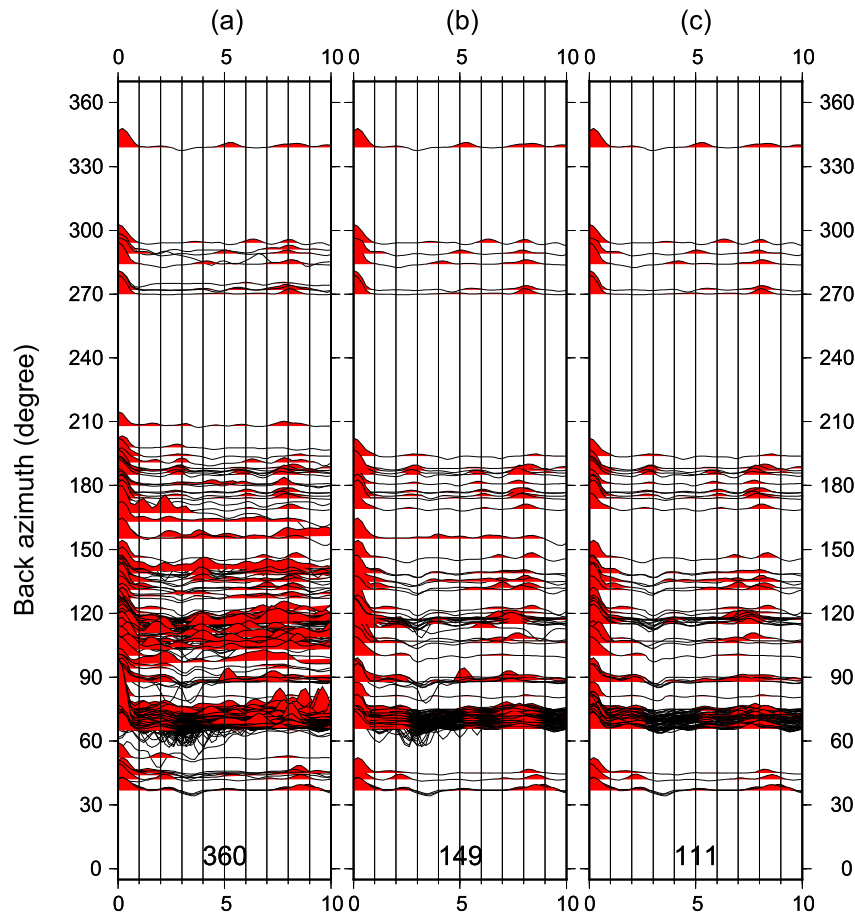


Figure 2. Example of the quality control process for receiver functions (RFs) at station DKL21. (a) The full set of 360 observed RFs are plotted versus backazimuth. (b) The 149 residual RFs after quality control steps 1 and 2. (c) The final 111 RFs after harmonic stripping, quality control step 3, in which only RFs that vary smoothly with azimuth are retained.

where we take $t_i = 0$ s and $t_f = 11$ s. If $D(j) > 0.06$, we reject the receiver function. The threshold (0.06) is chosen empirically so that obvious outliers are removed and we retain as many receiver functions as possible. What remains are observed receiver functions that vary smoothly in azimuth.

Figure 2 presents an example of the result of the quality control process for station DKL21 whose location is identified in Fig. 3. The original receiver functions from 360 earthquakes are presented in Fig. 2(a) separated by azimuth. Most receiver functions are from earthquakes at azimuths between about 40° and 200° , which are from the northeast to the south of the study region. Substantial disagreement among the receiver functions is apparent in Fig. 2(a). After quality control Steps 1 and 2, the number of receiver functions reduces to 149 as shown in Fig. 2(b). The 111 azimuthally smooth receiver functions that emerge from the harmonic analysis of Step 3 are shown in Fig. 2(c). After the quality control process is complete, we retain a total of 1145 receiver functions for the 22 stations along the profile.

2.1.4 Receiver function CMCP stacks

Shen *et al.* (2013a,b) advocated for the use of the function $A_0(t)$ from eq. (2) as representative of the azimuthally independent structure beneath the station. However, Fig. 2 shows that the distribution of earthquakes in our study produces receiver functions that lie primarily in the azimuthal range from 40° to 200° , so $A_0(t)$ may be

biased by azimuthally dependent structure near the station. Figure 3 further illustrates this point by presenting the locations of the Moho piercing points of P waves (or P to S conversion points) retained after quality control. Moho piercing points are computed by ray tracing from each earthquake through a model with P velocities from IASP91 (Kennett & Engdahl 1991) but with crustal thickness from Xu *et al.* (2014). The piercing points are predominantly to the east and southeast of the stations at which the receiver functions are observed and are characteristic of structures there rather than near the stations. For this reason, we use harmonic stripping only for quality control and not to produce the stacked receiver functions at the stations. Rather, we stack receiver functions along the observation profile at a set of 23 stacking locations lying at 20 km intervals (Fig. 3, black dots, numbered 1–23). We stacked (i.e. averaged) the receiver functions with Moho piercing points lying within 0.15° of each stacking location. We refer to this as the common Moho conversion point (CMCP) stacking method, which is somewhat similar to the CCP (common conversion point) stacking method (e.g. Dueker & Sheehan 1998). The weights used in stacking are shown in the inset panel in Fig. 3 showing nine square sub-boxes with sides of 0.1° . In each sub-box, we average all receiver functions with equal weight producing what we call a sub-box receiver function. Then the sub-box receiver functions are stacked (averaged) according to the weights presented in the inset panel where the central sub-box lies on the stacking location. The stacking locations together form what we call the ‘observation profile’.

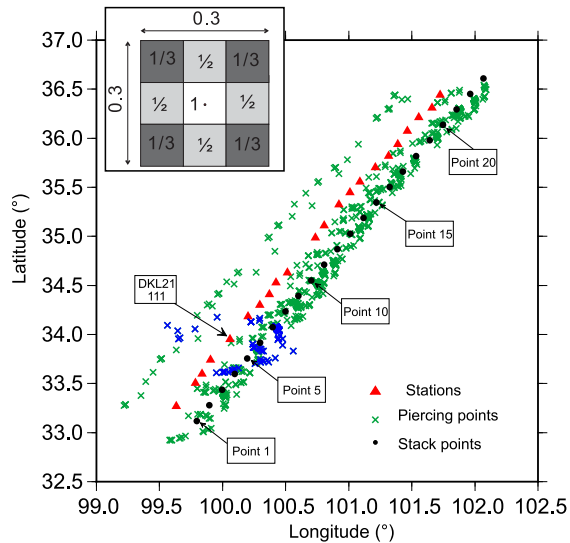


Figure 3. Red triangles mark the locations of the 22 stations along the observation profile and green crosses show Moho piercing (or conversion) points (red crosses) of the incident P waves. Blue crosses are Moho piercing points for station DKL21 (identified). The black dots indicate the stacking locations, which are separated by 20 km and numbered 1–23 (shown). The inset box contains the weights used to stack the receiver functions.

Figures 4(b) and (c) present the stacked receiver functions along the observation profile with locations identified by the location numbers 1–23. Figure 4(b) shows the stacked receiver function waveforms themselves and Fig. 4(c) shows the same information but with amplitude-dependent colour shading. The P and P -to- S converted phases from the Moho can be seen clearly along the profile. The delay time between the P and P -to- S converted phases from the Songpan–Ganzi block (SB) to the Qilian block (QL) varies from about 7 to 8 s. This delay time reduces northward along the stacking profile and becomes more complicated, showing a double peak at most locations north of stacking location 12. Additional complexities in the receiver functions also appear in Fig. 4, which are discussed later in the paper.

We also estimate uncertainties for each receiver function along the profile. First, we compute the standard deviation at each time among the receiver functions in each stacking sub-box. We then take the weighted average of these standard deviations to compute the uncertainty of the stacked receiver function, using the weights given in the inset panel of Fig. 3. An example of these one standard deviation uncertainties can be seen for location 13 as the grey shaded envelope in Fig. 5(a).

2.2 Rayleigh wave phase velocity

Xie *et al.* (2013) mapped phase velocities across eastern Tibet and surrounding regions for Rayleigh (8–65 s) and Love (8–44 s) waves using ambient noise tomography based on data from the Program for Array Seismic Studies of the Continental Lithosphere (PASSCAL) and the Chinese Earthquake Array (CEArray). In that study, uncertainties of the surface wave phase speeds were also obtained by performing eikonal tomography (Lin *et al.* 2009). We interpolate the Rayleigh wave phase speed and uncertainty curves beneath the stacking points, an example of which is shown in Fig. 5(b) for location 13. Rayleigh wave phase speeds increase from about 3.1 km s^{-1} at 8 s period to about 3.85 km s^{-1} at 65 s period, and the

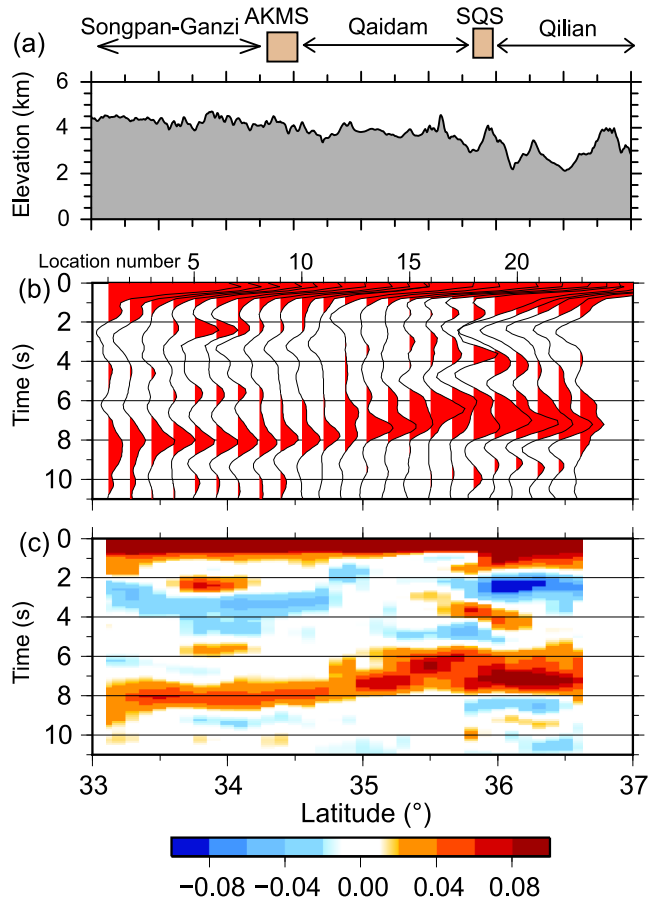


Figure 4. (a) The elevation along the observation profile. (b) Moho conversion point (MCP) stacked receiver functions are illustrated with red waveforms as a function of the stacking location number. (c) Smoothed colour-coded image of the receiver functions.

uncertainty also increases with the period. Other example Rayleigh wave phase speed curves are presented later in the paper.

2.3 Joint inversion of receiver functions and surface wave dispersion

Internal interfaces such as sedimentary basement and Moho are difficult to resolve based on the inversion of surface wave data alone. While surface wave dispersion constrains well the vertically averaged velocity profile, it only weakly constrains velocity interfaces and strong velocity gradients. Receiver functions have complementary strengths to surface wave data (e.g. Ozalaybey *et al.* 1997; Julia *et al.* 2000; Du *et al.* 2002; Li *et al.* 2008) and the joint inversion of surface wave dispersion with receiver functions may be more reliable than structures derived exclusively on either data set alone (e.g. Julia *et al.* 2003, 2005; Chang & Baag 2005; Shen *et al.* 2013a,b). Shen *et al.* (2013a) developed a non-linear Bayesian Monte-Carlo algorithm to estimate a V_s model by jointly interpreting Rayleigh wave dispersion and receiver functions as well as associated uncertainties. We apply this method here. We apply stacked receiver functions in the 0–11 s time band and Rayleigh wave phase speeds between 8 and 65 s period at 20 km intervals along the observation profile. This time band and period range provides information about the top 80 km of the crust and uppermost mantle. In the models presented here, both the inversion of surface wave data performed by Xie *et al.* (2013) and the joint inversions of surface wave data and

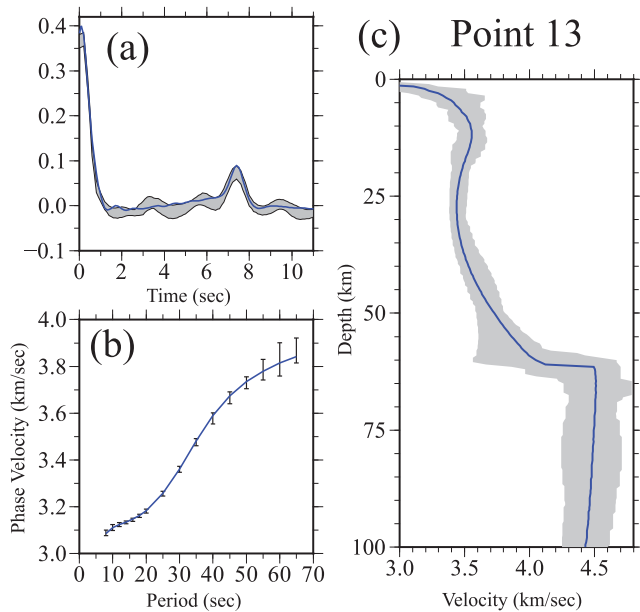


Figure 5. Example of data and inversion result at location number 13. (a) The observed receiver function (with uncertainty) is presented as the grey envelope. (b) The observed Rayleigh wave phase speed curve (with uncertainties) is plotted with one standard deviation error bars. (c) The full (grey) envelope of accepted models in the posterior distribution from the joint inversion of the receiver function and dispersion data with a smoothly varying crystalline crust (i.e. Model 1). The blue lines in (a) and (b) show the predicted data from the best-fitting model and the blue line in (c) presents the mean of the posterior distribution at each depth.

receiver functions presented for the first time here, we apply a V_p/V_s ratio of 1.75 in both the crust and uppermost mantle. We choose to fix this ratio primarily for consistency with the starting model (Xie *et al.* 2013). There is no doubt, however, that V_p/V_s varies with depth and along our observation profile. The V_p/V_s ratio trades off with crustal thickness and structures within the crust and, therefore, the depth to Moho and the amplitude and depth of structural features in the crust will depend on this choice.

3 CRUSTAL STRUCTURE ALONG THE PROFILE

3.1 Smooth starting model from surface waves alone

We start with the model of Xie *et al.* (2013), which is determined from Rayleigh and Love wave phase speed measurements alone determined from ambient noise tomography. (For the background to this study see: Shapiro *et al.* 2004; Bensen *et al.* 2007; Lin *et al.* 2008, 2009; Zheng *et al.* 2008; Yang *et al.* 2010, 2012; Ritzwoller *et al.* 2011; Zheng *et al.* 2011; Zhou *et al.* 2012). The model is composed of three layers stacked vertically with variable thicknesses but the crystalline crust is vertically smooth. The top layer is the sediments, which are isotropic ($V_s = V_{sv} = V_{sh}$) with constant velocity vertically. The middle layer is the crystalline crust, which is radially anisotropic ($V_{sv} \neq V_{sh}$). Each of V_{sv} and V_{sh} is given by five B-splines in the crystalline crust. The bottom layer is the radially anisotropic uppermost mantle in which V_{sv} is given by five B-splines and the difference between V_{sh} and V_{sv} is taken from an earlier model of the region (Shapiro & Ritzwoller 2002; Shapiro *et al.* 2004). Sedimentary thickness and Moho depth were free variables in the inversion for this model, which applied sev-

eral constraints including vertical crustal smoothness and positive jumps at the base of the sediments and crust. For the purposes here, we only use the V_{sv} part of the model at all depths and set the model to be isotropic ($V_s = V_{sv} = V_{sh}$) because we only invert Rayleigh waves and receiver functions. The V_p/V_s ratio both in the crust and mantle is set to 1.75.

A plot of V_{sv} as a function of depth along the observing profile is presented in Fig. 6(a). In this model the crust thins slowly and continuously to the north from about 61.5 km in the Songpan–Ganzi block to 51.5 km in the Qilian block. More prominently, in the Songpan–Ganzi block mid-crustal V_{sv} is very slow, much slower than in the Qilian block. Hacker *et al.* (2014) argue that such slow shear velocities must be caused by partial melt in the middle crust.

Although receiver functions were not used in the construction of the model of Xie *et al.* we compute synthetic receiver functions and present them in Figs 7(a) and (b), designed to be compared with the observed receiver functions in Figs 4(b) and (c). The timing of the Moho P -to- S converted phases on the synthetic receiver functions is similar to the observed receiver functions but other aspects of the synthetics and observations are quite different. First, the positive swing on the synthetic P -to- S converted phase is too broad, which is caused by a strong vertical velocity gradient both above and below the Moho in the model. Second, internal crustal structures are reflected in the observed receiver functions that are entirely missing in the synthetics. Such structures are apparent in Fig. 7(c), which presents the difference between the observed and synthetic receiver functions. Third, there are also complexities in the observed receiver functions near the P -to- S converted phase north of 35° latitude that are not apparent in the synthetics. We measure reduced χ^2 misfit on the interval between t_i and t_f for each of the 23 stacking locations as follows:

$$\chi_{\text{location}}^2 = \frac{1}{t_f - t_i} \int_{t_i}^{t_f} \left(\frac{\text{RF}^{\text{obs}}(t) - \text{RF}^{\text{pred}}(t)}{\sigma^2(t)} \right)^2 dt \quad (4)$$

where RF^{obs} and RF^{pred} are the observed and predicted receiver functions at the location, respectively, σ is the standard deviation at the location and we take $t_i = 2$ s and $t_f = 8$ s. These location specific reduced χ^2 values are then averaged over the 23 locations to determine the total reduced χ^2 , which is 5.1 for the starting model. These results suggest, not surprisingly, that there are complexities in the structure of the crust that are missing in the vertically smooth crustal model of Xie *et al.*

3.2 Joint inversion of surface waves and receiver functions with a vertically smooth crystalline crust: Model 1

To begin to model the complexities in crustal structure implied by the receiver functions and inferred in Section 3.1, we first perform a joint inversion of the Rayleigh wave dispersion data and the receiver functions at each location along the profile but continue with the constraint that the model is vertically smooth in the crystalline crust. We refer to this model as having resulted from the vertically smooth joint inversion or as Model 1. Data such as those shown in Figs 5(a) and (b) are inverted jointly using the method described by Shen *et al.* (2013a,b). The starting model is the model of Xie *et al.* (2013) and we adopt the parametrization of this model with three modifications: (1) the model is isotropic at all depths (there is no radial anisotropy) such that $V_s = V_{sv}$, (2) we use seven B-splines for V_{sv} in the crust rather than five and (3) we represent sedimentary velocities as a linear monotonically increasing function of depth rather than a constant. Importantly, as crystalline crustal structure

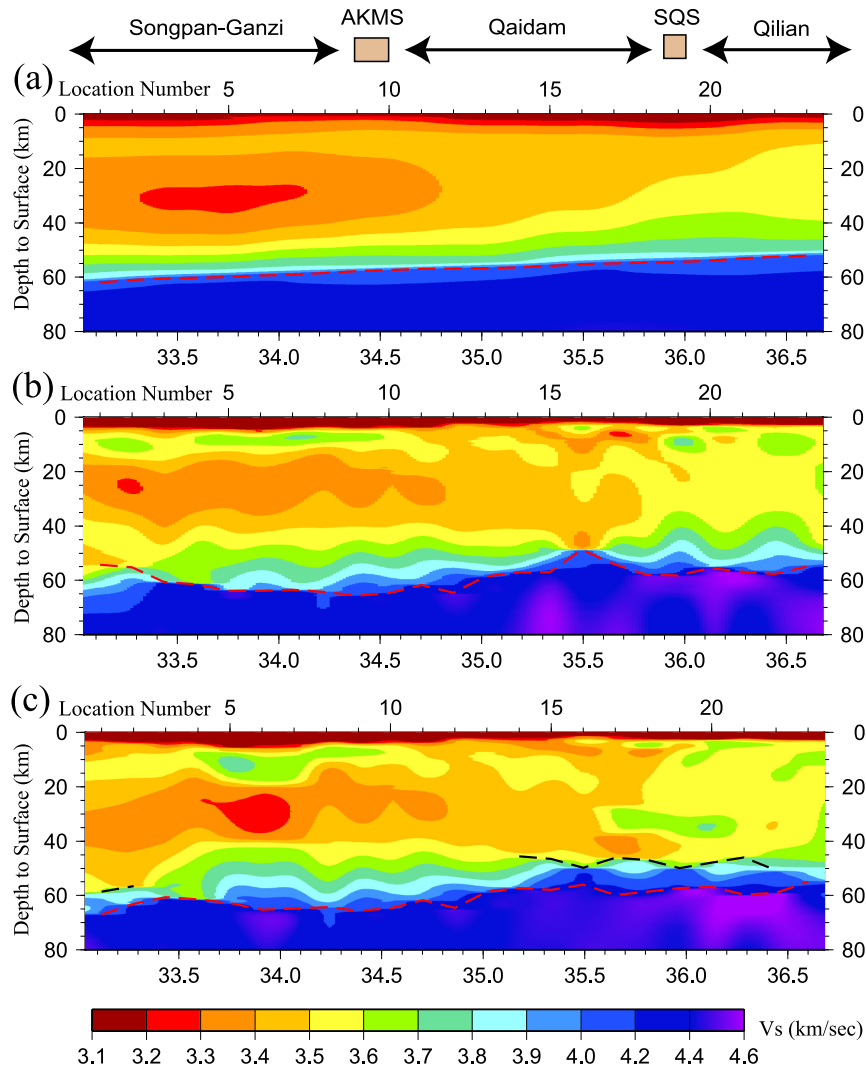


Figure 6. The three models discussed here, all are V_s (km s^{-1}). (a) The starting model from Xie *et al.* (2013) constructed with Rayleigh wave dispersion data alone. (b) Model 1, which results from the joint inversion of receiver functions and Rayleigh wave dispersion without discontinuities in the crystalline crust. (c) Model 2, which results from the joint inversion of receiver functions and Rayleigh wave dispersion with discontinuities in the crystalline crust at the locations specified in Table 1.

is represented with B-splines, although larger in number than in the model of Xie *et al.* in this inversion the crystalline crust still is constrained to be smooth vertically. In Section 3.3, this constraint is broken in order to introduce internal crustal interfaces that appear to be needed in order to fit the receiver function data.

We perform the inversion with a Bayesian Monte Carlo method aimed to fit the Rayleigh wave dispersion and receiver functions jointly and equally well at each location along the observation profile. Uncertainty estimates in each type of data weight the relative influence of each data type in the likelihood function (i.e. misfit) and the inversion results in a posterior distribution of models that fit the data acceptably at each depth. Figure 5(c) shows the results of the inversion at Point 13 along the observation profile, presented with a grey corridor that represents the full width of the posterior distribution at each depth. The blue line is the mean of the posterior distribution at each depth.

The mean value of the posterior distribution for V_s at each depth along the observation profile is presented in Fig. 6(b). Compared with the starting model from Xie *et al.* (2013) determined from surface wave data alone in Fig. 6(a), vertical variations in Model

from 1 are sharper; for example, the mid-crustal velocities in the Songpan–Ganzi block are confined to a narrower depth range, and are faster and overlain by a thin veneer of higher velocities at about 10 km depth. There are higher velocities in the lowermost crust (50–60 km) bracketing the Kunlun fault and the mid-crustal velocities in the Qilian block are generally faster although very low velocities appear in the lowermost crust south of the south Qilian suture.

Figures 8(a) and (b) present the synthetic receiver functions computed from Model 1. A comparison, in particular, between the observed receiver functions in Fig. 4(c) and the synthetics in Fig. 8(b) illustrates the improvement in fit via the introduction of vertically smooth internal crustal structures that nevertheless produce receiver function arrivals between the direct P arrival and the P -to- S conversion. Figure 8(c) quantifies this comparison by presenting the difference between the observed and synthetic receiver functions. Contrasting Fig. 8(c) with Fig. 7(c) shows that the fit to the receiver functions is greatly improved compared with the model of Xie *et al.* even though the model remains vertically smooth in the crust. The overall χ^2 , defined by eq. (4), is 1.4, which represents a 72 per cent reduction in the variance relative to the starting model. Therefore,

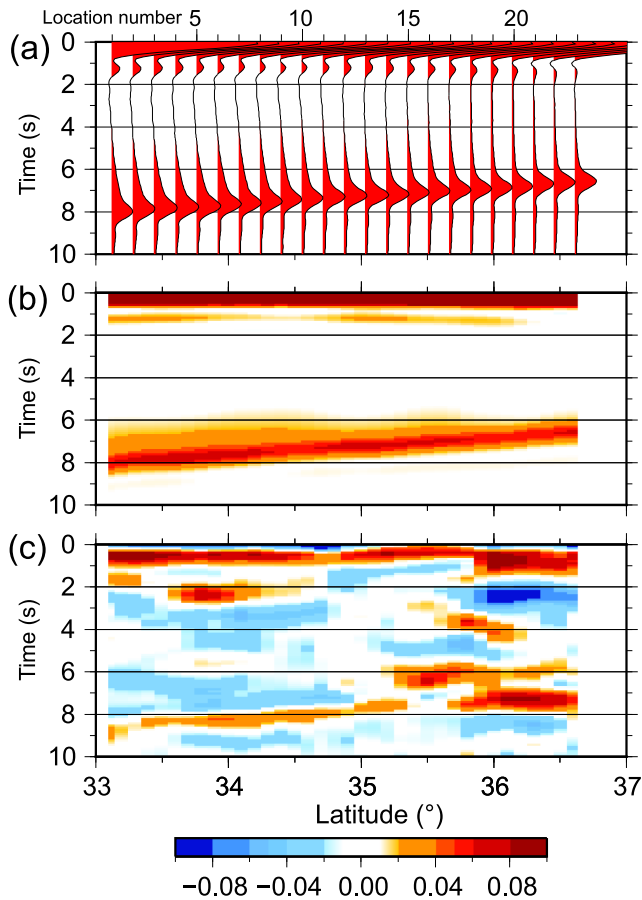


Figure 7. (a) The computed receiver functions (RFs, red lines) from the starting model of Xie *et al.* (2013). (b) A smoothed colour-coded image of the computed RFs. (c) The difference between computed RFs and observed RFs.

the introduction of receiver functions in the joint inversion is advisable even when retaining a vertically smooth model.

Nevertheless, there remain considerable differences between the observed and synthetic receiver functions, particularly in the boxes marked (A) and (B) in Fig. 8(c). This can be seen more clearly in Fig. 9, which presents vertical profiles beneath Point 6 (box A) and Point 18 (box B) from Model 1 as the red lines in Figs 9(a) and (d), respectively. (Blue lines and the corridor of accepted models are discussed later, in Section 3.3.) Figures 9(a) and (d) (red lines) illustrate how the receiver functions at these two points are misfit by Model 1. The misfit in the receiver function near Point 6 is somewhat subtle, but at Point 18 the double peak between 6 and 8 s cannot be fit with this model and neither can the swings in the receiver function between 3 and 5 s.

For these reasons, it is necessary to move beyond vertically smooth crystalline crustal models in order to fit the receiver function data in Tibet at least in some (perhaps most) locations. Interfaces within the crust are needed, therefore, to fit the receiver function data in detail. This is a different conclusion than drawn by Shen *et al.* (2013b,c) for the western and central US, where vertically smooth crystalline crustal models were found to suffice to fit surface wave dispersion and receiver function data jointly except in isolated areas across this region. Of course, the crust is much thinner in the US than in our region of study.

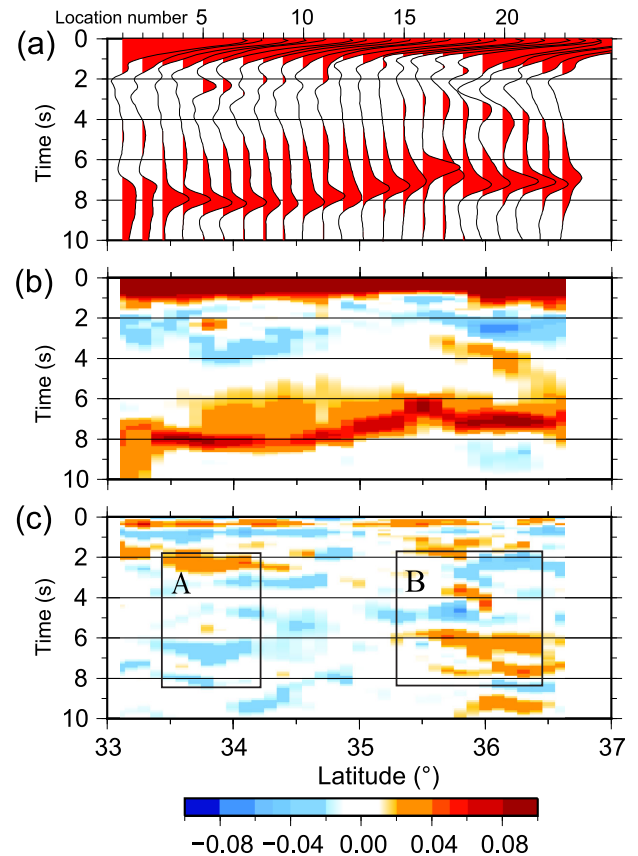


Figure 8. Similar Fig. 7, but here receiver functions are computed using Model 1, which results from the joint inversion of receiver functions and Rayleigh wave dispersion without discontinuities in the crystalline crust. The boxes denoted (A) and (B) identify areas in which we particularly seek to improve the fit to the receiver functions.

3.3 Joint inversion of surface waves and receiver functions with a layered crystalline crust: Model 2

To move beyond the vertically smooth crystalline crustal model from the joint inversion presented in Section 3.2 (Figs 6(b) and 8), we introduce different mid-crustal discontinuities in Regions 1, 2 and 3, which are identified in Table 1.

Region 1 encompasses latitudes between about 33.6° and 34.2° , locations numbered 5–7, which lie in the northern part of the Songpan–Ganzi block to the Kunlun fault. In this region we introduce two mid-crustal discontinuities to the starting model, one at 20 km depth and one at 40 km depth and allow a constant velocity perturbation between them. The depths of these discontinuities and the amplitude of the perturbation are introduced as free variables in the inversion. The result at Point 6, which is contained in Region 1, is shown in Fig. 9(c). The grey envelope denotes the full width of the posterior distribution, the blue line marks the mean of the posterior distribution at each depth and the red line is the mean of the posterior distribution of Model 1 (Section 3.2). The introduction of these three degrees of freedom acts to restrict the depth extent of the low velocity zone (LVZ) in the central crust, increase the shear wave speed across most of the lower crust and reduce crustal thickness relative to Model 1. The result is a considerably better fit to the receiver function (blue line in Fig. 9a), particularly the *P*-to-*S* Moho conversion phase that appears near 8 s.

Region 2 lies between latitudes of about 35.6° and 36.2° , locations numbered 17–20, which is the northern part of the Qaidam block to

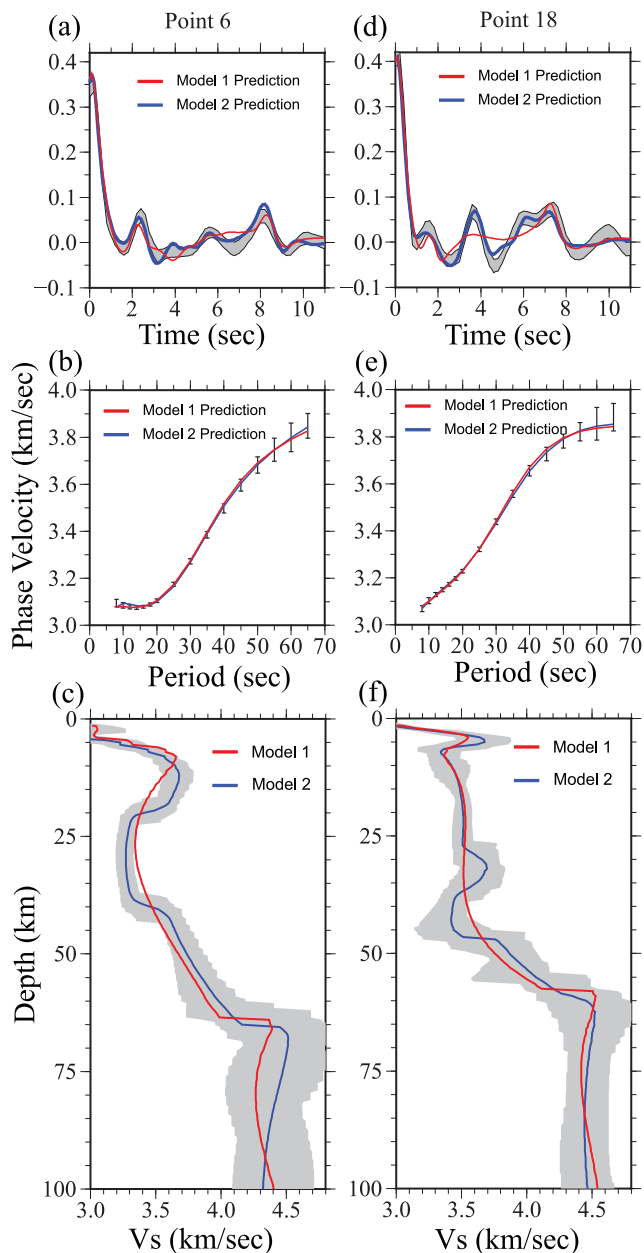


Figure 9. Similar to Fig. 5 in which example data and fits to receiver functions are presented for two sample points: 6 (left column) and 18 (right column), which lie in the boxes marked (A) and (B) in Fig. 8. Fits to the observed receiver functions and Rayleigh wave phase velocities by both Models 1 and 2 are presented as red and blue lines, respectively, in (a), (b), (d) and (e). Red and blue lines in (c) and (f) represent the best-fitting model of Model 1 (red) and Model 2 (blue). The full envelope of accepted models in the inversion with crustal discontinuities (Model 2) is shown in (c) and (f).

the southern Qilian block, encompassing the southern Qilian suture. In this region the receiver functions are more complicated than elsewhere along the profile, and we introduce six degrees of freedom to the starting model. First, we introduce two mid-crustal discontinuities at 30 km and 40 km depth and allow a constant velocity perturbation between them. These three degrees of freedom allow for a HVZ in the central crust to develop. Second, we also allow for a ‘doublet Moho’ by introducing three more degrees of freedom to produce a linear velocity gradient in the lowermost crust (or

uppermost mantle) with variable depth and upper and lower shear velocities. The result at Point 18, which is contained in Region 2, is shown in Fig. 9(f). An HVZ is introduced in the middle crust between depths of about 30–40 km and there are two prominent discontinuities that compose the doublet Moho, one near 45 km and another nearer to 60 km depth with a linear velocity gradient between these depths. The result is a much better fit to the receiver function (blue line in Fig. 9d), including the double *P*-to-*S* Moho conversion phase that appears between 6 and 8 s, the positive swing near 3.5 s and the negative swings near 2.5 and 4.5 s.

Finally, Region 3 comprises a discontinuous set of locations numbered 1–2, 14–16 and 21–22. In these locations we allow for a doublet Moho. Two of these ranges of points bracket Region 2, which also contains a doublet Moho, and the third occurs at the southern end of the observation profile. The locations with a doublet Moho are made clearer later in Fig. 11, discussed later in the paper.

The receiver functions in Figs 10(a) and (b) computed with the introduced mid-crustal discontinuities of Model 2 fit the observed receiver functions in Figs 4(b) and (c) much better than either the starting model or Model 1, particularly in Box B. The total reduced χ^2 (eq. 3) is 0.9, which is a 82 per cent variance reduction relative to the starting model and a 36 per cent variance reduction relative to Model 1. The residual is small across most of the profile with the principal exception at times greater than about 7 s near the south Qilian suture (Box B), which we believe may be due to further layering in the uppermost mantle near the Qilian block.

Model 2, the model from the joint inversion with the layers introduced in the crystalline crust, is shown in Fig. 6(c). The LVZ near 34° latitude in the Songpan–Ganzi block has been accentuated further by lowering the minimum velocities and the uppermost and lowermost crust has correspondingly been made faster. More substantially, the model between 35.5° and 36.2° latitude, bracketing the south Qilian suture, now has an HVZ introduced near a depth of 35 km with a doublet Moho (as shown).

In summary, the surface wave dispersion data and receiver functions can be fit with a smooth crustal model across part of the observation profile, principally between location numbers 8–14 in the middle of the observation profile, but not in Regions 1–3 (Table 1). In these regions, crustal discontinuities must be introduced to fit the receiver functions. In Region 1, this produces a vertically narrower LVZ with a lower shear wave speed minimum. Region 2 is more complicated, requiring an HVZ in the middle crust. Beneath Regions 2 and 3 a doublet Moho at depths of about 50–60 km provides a significant improvement in fit to the receiver functions.

4 DISCUSSION

4.1 Mid-crustal LVZ in the Songpan–Ganzi block: evidence for partial melt

Crustal LVZs have been identified across Tibet by a number of studies (e.g. Kind *et al.* 1996; Cotte *et al.* 1999; Rapine *et al.* 2003; Shapiro *et al.* 2004; Xu *et al.* 2007; Caldwell *et al.* 2009; Guo *et al.* 2009; Li *et al.* 2009; Yao *et al.* 2008, 2010; Acton *et al.* 2010; Jiang *et al.* 2011). Yang *et al.* (2012) summarize evidence from surface waves for a mid-crustal LVZ across much of Tibet. Such evidence generally supports the internal deformation model of Tibetan evolution where the medium is treated as a non-rigid continuum (e.g. England & Houseman 1986; England & Molnar 1997) and may particularly favour ductile ‘channel’ flow in the

Table 1. Locations and types of crustal discontinuities.

Region number	Structures introduced	Location numbers	Latitude range
1	Slow mid-crustal layer	5–7	33.6°–34.2°
2	Moho doublet + fast mid-crustal layer	17–20	35.6°–36.2°
3	Moho doublet	1–2 14–16 21–22	33.1°–33.3° 35.1°–35.6° 36.2°–36.5°

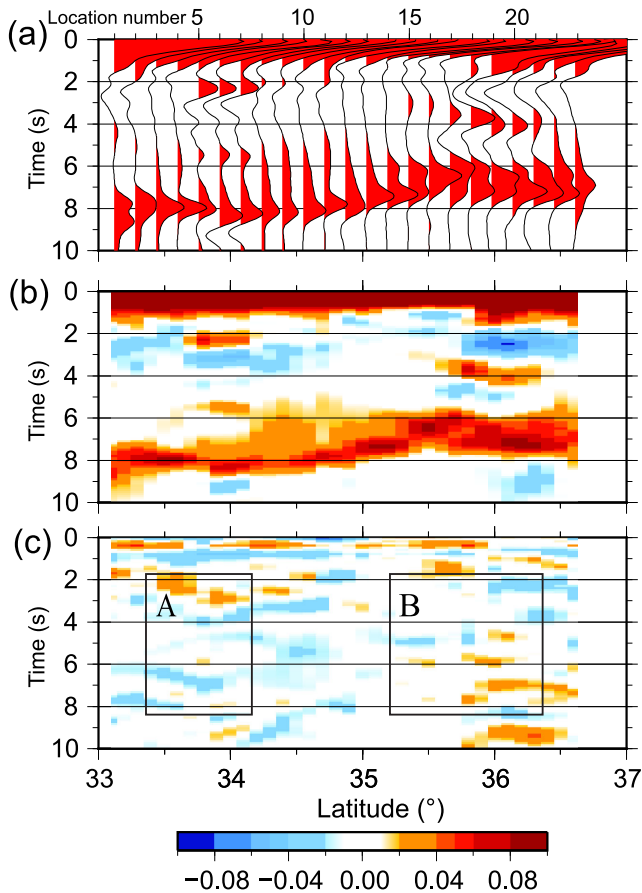


Figure 10. Similar Figs 7 and 8, but here RFs are computed using Model 2, which results from the joint inversion of receiver functions and Rayleigh wave dispersion with specified discontinuities in the crystalline crust. The boxes denoted (A) and (B) are described in Fig. 8.

middle and/or lower crust (e.g. Bird 1991; Clark & Royden 2000; Searle *et al.* 2011). Based on the more recent model of crustal shear velocities of Xie *et al.* (2013), our starting model presented along the observation profile in Fig. 6(a), Hacker *et al.* (2014) argue that the low mid-crustal shear velocities across Tibet are indicative of partial melt. In the region of study, if we identify the LVZ as shear wave speeds (V_{sv}) below 3.4 km s^{-1} in the middle crust, then the LVZ extends from the Songpan–Ganzi block through the Kunlun fault into the Qaidam block as far north as 34.9° (Fig. 6a). In this region, the V_p/V_s ratio was identified by Xu *et al.* (2014) to be greater than 1.75. As elsewhere in Tibet, block or terrane boundaries do not appear to obstruct crustal LVZs in the middle to lower crust (e.g. Yang *et al.* 2012; Jiang *et al.* 2014). Here, we ask the question whether the introduction of receiver functions in Region 1 (identified in Table 1) in the inversion increases or decreases the likelihood of partial melt in the middle crust.

First, in the results of the joint inversion of Rayleigh wave dispersion and receiver functions with an imposed crustal vertical smoothness constraint (Model 1, Fig. 6b), the shear velocities in the middle crust actually rise compared to the starting model constructed with surface wave data alone (Fig. 6a). This somewhat reduces the likelihood of partial melt in the middle crust. This rise occurs because the attempt to fit the receiver functions with a vertically smooth crystalline crust increases crustal thickness, which reduces predicted Rayleigh wave speeds in the period band sensitive to the middle and lower crust and the increased mid-crustal shear wave speeds compensate. Minimum V_{sv} speeds in the middle crust beneath the Songpan–Ganzi block in Model 1 mostly lie between 3.3 and 3.4 km s^{-1} but are somewhat lower in the starting model (Fig. 6a).

However, when two mid-crustal discontinuities are introduced in the joint inversion (Model 2, Fig. 6c) in order to improve the fit to the receiver function data, then the LVZ is accentuated in the middle crust beneath the Songpan–Ganzi block. In particular, the transitions to the LVZ from above and below are sharper, the LVZ is confined to a narrower depth range (20–40 km as opposed to 15–45 km) and the minimum shear wave speeds are lowered by about 0.1 km s^{-1} , which makes partial melt more somewhat more likely than in the model of Xie *et al.* (2013). Moreover, by introducing the mid-crustal discontinuities to improve the fit to the receiver functions, sharp transitions are obtained within and outside of the mid-crustal LVZ beneath the northern Tibet. As proposed by Hacker *et al.* (2014), the melt produced in the middle and lower crust may have accumulated atop the melted zone at 20–30 km beneath the surface of the high plateau. The sharp reduction in V_s we observe above the LVZ at a depth of ~ 20 km may be due to such a mechanism, serving as more evidence in favour of partial melt in addition to the minimum shear wave speeds.

Consequently, improving the fit to receiver functions by introducing internal crustal discontinuities modifies the shape and nature of LVZ beneath northern Tibet but does not reduce the likelihood of mid-crustal partial melt. Rather, it results in a slight increase in the likelihood of mid-crustal partial melt.

4.2 Mid-crustal HVZ in the Qilian block: coincident with HP/UHP metamorphism

The Qilian Caledonian orogenic belt is believed to be the product of the convergence and collision between the north China Craton with the Qilian and Qaidam terranes during the Early Palaeozoic Era (Yang *et al.* 2001). UHP metamorphic rocks are found along and near the south Qilian suture and several geological and tectonic models have been proposed to explain the origin of these rocks (Wang & Chen 1987; Yang *et al.* 1994, 2002; Song *et al.* 2006, 2009; Yin *et al.* 2007; Zhang *et al.* 2009). The crust near the south Qilian suture is known to be geophysically complicated, possessing highly variable V_p/V_s ratios (e.g. Xu *et al.* 2014), high and variable residual Bouguer gravity anomalies (EGM2008; Pavlis *et al.* 2012) and complicated receiver functions (e.g. Vergne *et al.* 2002; Xu

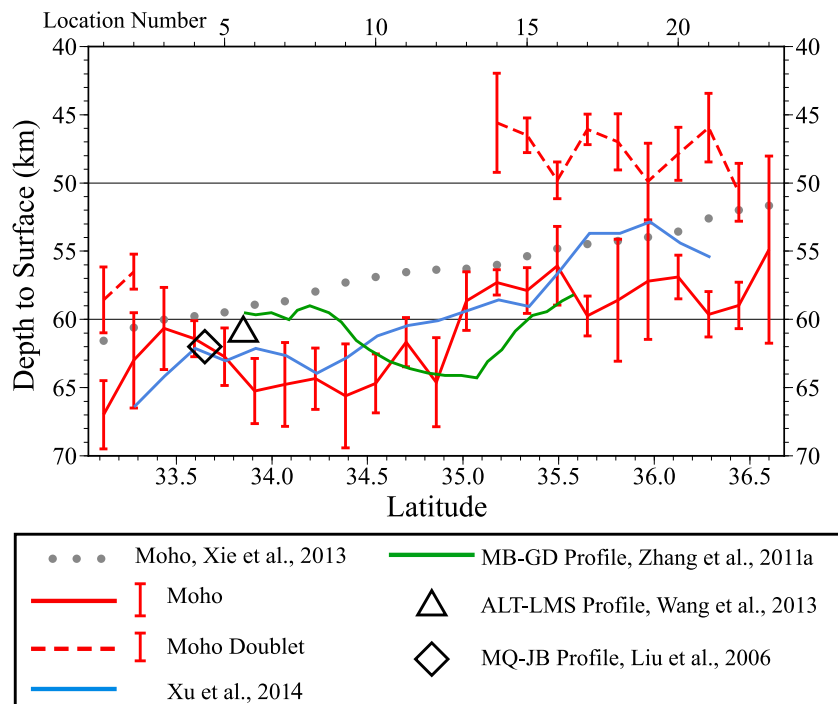


Figure 11. Our estimates of crustal thickness are presented with red error bars (1 standard deviation). Where we infer a doublet Moho the lower interface is interpreted as Moho (red solid line) and the upper interface is identified with the red dashed line. Crustal thickness from Xie *et al.* (2013) is presented with grey dots, from the receiver function study of Xu *et al.* (2014) is presented with the blue line and from the deep seismic sounding study of Zhang *et al.* (2011a) with the green line. The symbols (diamond and triangle) mark crustal thickness estimates from crossing lines (Liu *et al.* 2006; Wang *et al.* 2013).

et al. 2014). Our crustal model adds to this picture of crustal complexity by introducing a prominent high velocity anomaly at a depth of about 35 km that brackets the south Qilian suture (latitudes from 35.6° to 36.2°) directly below and adjacent to surface outcrops of UHP metamorphic rocks. We believe that the most likely interpretation is that this anomaly results from compositional heterogeneity, presumably of relatively enriched mafic rocks. Whether and how this anomalous structure relates to the UHP metamorphic rocks of the areas remains an area for further investigation.

4.3 The ‘Doublet Moho’: evidence for a transitional lower crust bracketing the south Qilian suture

A doublet Moho has been observed in earlier studies in at least two different locations beneath the Lhasa terrane in southern Tibet (Kind *et al.* 2002; Nabelek *et al.* 2009; Li *et al.* 2011) and has been interpreted by Nabelek *et al.* (2009) to be caused by eclogitized lower crust from the Indian Plate underplating the Tibetan crust. As Fig. 6(c) shows, we infer a doublet Moho to bracket the south Qilian suture at latitudes from about 35.1° to 36.5°. Part of the doublet Moho underlies the mid-crustal high velocity body discussed in Section 4.2. The depth to both discontinuities that compose the doublet Moho are presented more clearly in Fig. 11.

The doublet Moho extends from depths of between 45–50 km and 55–65 km and encompasses an anomalously strong vertical velocity gradient. We interpret the latter discontinuity as classic Moho because beneath it lies shear wave speeds consistent with mantle rocks. Within the transition zone between these two discontinuities, shear wave speeds lie between about 3.8 and 4.2 km s⁻¹. The high end of this range is only slightly faster than the lower crust south of this region where there is a single Moho, in the Qaidam and Songpan–Ganzi blocks; thus, the higher velocities rise up to shallower depths

beneath the doublet Moho than further south. Thus, we do not find evidence that the lower crust encompassed by the doublet Moho is compositionally distinct from the lower crust elsewhere along the observation profile, but the lower crustal composition extends to shallower depths.

The cause of the doublet Moho is not clear. One possibility is that there is no distinct crust–mantle division, but rather crustal and mantle rocks are interlayered in this region. Searle *et al.* (2011) propose that the principal mineralogical composition of the Tibetan lower crust is granulite and eclogite with some ultramafic restites. Yang *et al.* (2012) argue that shear wave speeds of eclogite are expected to be about 4.4 km s⁻¹ at the temperature and pressure conditions of the lower crust within Tibet. *In situ* lower crustal shear wave speeds all along the observing profile are significantly lower than this value so that the lower crust may be only partially eclogitized if eclogitization does indeed occur. Schulte-Pelkum *et al.* (2005) estimate that 30 per cent of the lower crust undergoes eclogitization in southern Tibet. Thus, an increasing fraction of eclogite versus granulite with depth may explain the vertical velocity gradient in the lower crust beneath the entire observation profile. What is unusual and requires further study is that the high shear wave velocities are compressed into a much narrower depth range in the doublet Moho regions than elsewhere along the observation profile.

4.4 Crustal thickness and stepwise crustal thickening: comparison with previous studies

The crust and upper mantle in different parts of the northeastern Tibetan plateau have been studied by a range of controlled source seismic experiments (e.g. Zhang *et al.* 2011b), many of which are identified in Fig. 1. Our estimate of crustal thickness and its uncertainty are presented in Fig. 11 as red error bars and two lines.

The dashed red line appears where we estimate a doublet Moho and indicates the shallower of the two discontinuities. The lower of the two discontinuities is indicated with a solid line and we take this to indicate crustal thickness. Crustal thickness averages 63.8 km (± 1.8 km) south of about 35° latitude and 57.8 km (± 1.4 km) north of this latitude, where the listed uncertainties are the standard deviation of the mean values south and north of this latitude. In fact, our results are consistent with a step-Moho at about 35° latitude. The location of the step is not coincident with the Kunlun fault, but is located about 50 km north of it. Rather it appears to be related to the termination of the mid-crustal LVZ that we find extends from the Songpan–Ganzi block into the Qaidam block as have other researchers (e.g. Jiang *et al.* 2014). Electromagnetic studies have also found that mid-crustal high conductivity features interpreted as melt extend north beyond the Kunlun fault (Le Paper *et al.* 2012).

Other studies have also inferred discrete steps in Moho in northern Tibet based on receiver function studies; some are considerably west of our observation profile (e.g. Zhu & Helmberger 1998) but others are quite close (e.g. Vergne *et al.* 2002). Vergne *et al.* argue that the stairsteps in Moho are located beneath the main, reactivated Mesozoic sutures in the region and take this as evidence against partial melt in the middle crust. We find, however, that the Moho step lies between the main sutures within our observation profile and appears to coincide with a change in middle crustal structure. In fact, it appears to lie near the northern edge of the mid-crustal LVZ, which we follow Hacker *et al.* (2014) to interpret as being caused by partial melt in the middle crust. We posit, therefore, that the staircase structure of Moho is consistent with a ductile middle crust and partial melt in the Tibetan crust.

Figure 11 presents crustal thickness estimates from other studies in the region for comparison with ours. Crustal thickness from the surface wave inversion of Xie *et al.* (2013), our smooth starting model which was based exclusively on the surface wave data we use here, slowly and continuously thins northward but is everywhere about 5 km thinner than our estimates as shown by the grey dotted line in Fig. 11. The introduction of receiver functions causes the crust in our model to thicken along the entire observation profile relative to the starting model and bifurcate into a thicker southern zone that steps discontinuously to a thinner northern zone.

Xu *et al.* (2014) used two methods to estimate crustal thickness based on the *P*-wave data we use to produce receiver functions: *PS* migration and *H–k* stacking. We average their crustal thickness estimates and present them in Fig. 11 as the blue line. These estimates typically agree within one standard deviation with our results but vary more smoothly with latitude and do not as clearly show the step-Moho that we estimate. Two other cross-profiles, the MQ-JB (Liu *et al.* 2006) and the ALT-LMS (Wang *et al.* 2013) shown in Fig. 1, exhibit similar crustal thickness at the intersections with our profile. There are greater differences with the active source crustal thickness estimates of Zhang *et al.* (2011a), presented as the green line in Fig. 11, which is more nearly constant with latitude.

5 CONCLUSIONS

The results presented here highlight the significance of crustal layering in Tibet and the importance of parametrizing such layering in models of the Tibetan crust. Although on some intervals along the observation profile a vertically smooth crust is consistent with both data sets, across most of the observation profile two types of layering are required. First, there is the need for a discrete LVZ or HVZ formed by two discontinuities in the middle crust. Second, there

is also the need for a doublet Moho formed by two discontinuities from 45–50 km to 60–65 km depth connected by a linear velocity gradient in the lowermost crust.

After modifying the model parametrizing by introducing these structural variables, we find that the final model (Model 2) possesses the following characteristics. (1) The model has a mid-crustal LVZ that extends from the Gongpan–Ganzi block through the Kunlun suture into the Qaidam block consistent with partial melt and ductile flow. (2) There is also a mid-crustal HVZ bracketing the south Qilian suture that is coincident with UHP metamorphism of surface rocks that are believed to reflect deep crustal subduction in the Palaeozoic. (3) Additionally, the model possesses a doublet Moho extending from the Qaidam to the Qilian blocks that probably reflects increased mafic content with depth in the lowermost crust perhaps caused by a gradient of eclogitization. (4) Crustal thickness is consistent with a step-Moho that jumps discontinuously from 63.8 km (± 1.8 km) south of 35° to 57.8 km (± 1.4 km) north of 35°, coinciding with the northern terminus of the mid-crustal LVZ that penetrates through the Kunlun suture into the Qaidam block.

We present these results as a guide to future joint inversions across a much larger region of Tibet. As long as crustal models are suitably parametrized, historical data sets from PASSCAL and CEArray deployments, such as those employed by Yang *et al.* (2012) and Xie *et al.* (2013), as well as new deployments can be used for the joint inversion of surface wave data and receiver functions to reveal more accurate crustal structures across Tibet.

ACKNOWLEDGEMENTS

The paper is dedicated to the memory of Prof Zhongjie Zhang (1964–2013). The authors are grateful to Donald Forsyth and an anonymous reviewer for insightful comments that improved this paper. We appreciate the constructive suggestions made by Prof. Xiaobo Tian, Xinlei Sun, Dr. Haiyan Yang and Zhenbo Wu, and the field work with Dr Changqing Sun and Fei Li. We gratefully acknowledge the financial support of State Key Laboratory of Isotope Geochemistry (SKBIG-RC-14-03) and the National Science Foundation of China (41021063) which supported the first author's visit to the University of Colorado for a period of six months. Aspects of this research were supported by NSF grant EAR-1246925 at the University of Colorado at Boulder. The facilities of IRIS Data Services, and specifically the IRIS Data Management Center, were used for access to waveforms, related metadata and/or derived products used in this study. IRIS Data Services are funded through the Seismological Facilities for the Advancement of Geoscience and EarthScope (SAGE) Proposal of the National Science Foundation under Cooperative Agreement EAR-1261681. This work utilized the Janus supercomputer, which is supported by the National Science Foundation (award no. CNS-0821794), the University of Colorado at Boulder, the University of Colorado Denver and the National Center for Atmospheric Research. The Janus supercomputer is operated by the University of Colorado at Boulder.

REFERENCES

- Acton, C.E., Priestley, K., Gaur, V.K. & Rai, S.S., 2010. Group velocity tomography of the Indo-Eurasian collision zone, *J. geophys. Res.*, **115**, B12335, doi:10.1029/2009JB007021.
- Ammon, C.J., 1991. The isolation of receiver effects from teleseismic *P* waveforms, *Bull. seism. Soc. Am.*, **81**(6), 2504–2510.
- Ammon, C.J., Randall, G.E. & Zandt, G., 1990. On the nonuniqueness of receiver function inversions, *J. geophys. Res.*, **95**(B10), 15 303–15 318.

- Bao, X. *et al.*, 2015. Two crustal low-velocity channels beneath SE Tibet revealed by joint inversion of Rayleigh wave dispersion and receiver functions, *Earth planet. Sci. Lett.*, **415**, 16–24.
- Bensen, G.D., Ritzwoller, M.H., Barmin, M.P., Levshin, A.L., Lin, F., Moschetti, M.P., Shapiro, N.M. & Yang, Y., 2007. Processing seismic ambient noise data to obtain reliable broad-band surface wave dispersion measurements, *Geophys. J. Int.*, **169**, 1239–1260.
- Bird, P., 1991. Lateral extrusion of lower crust from under high topography, in the isostatic limit, *J. geophys. Res.*, **96**, 10275–10286.
- Bodin, T., Sambridge, M., Tkalčić, H., Arroucau, P., Gallagher, K. & Rawlinson, N., 2012. Transdimensional inversion of receiver functions and surface wave dispersion, *J. geophys. Res.*, **117**, B02301, doi:10.1029/2011JB008560.
- Caldwell, W.B., Klemperer, S.L., Rai, S.S. & Lawrence, J.F., 2009. Partial melt in the upper-mantle crust of the northwest Himalaya revealed by Rayleigh wave dispersion, *Tectonophysics*, **477**, 58–65.
- Chang, S. & Baag, C., 2005. Crustal structure in Southern Korea from joint analysis of teleseismic receiver functions and surface-wave dispersion, *Bull. seism. Soc. Am.*, **95**, 1516–1534.
- Chen, W., Chen, C. & Nabelek, J., 1999. Present-day deformation of the Qaidam Basin with implications for intra-continental tectonics, *Tectonophysics*, **305**, 165–181.
- Chen, M., Huang, H., Yao, H., Hilst, R. & Niu, F., 2014. Low wave speed zones in the crust beneath SE Tibet revealed by ambient noise adjoint tomography, *Geophys. Res. Lett.*, **41**(2), 334–340.
- Clark, M.K. & Royden, L.H., 2000. Topographic ooze: Building the eastern margin of Tibet by lower crustal flow, *Geology*, **28**, 703–706.
- Cotte, N., Pederson, H., Campillo, M., Mars, J., Ni, J.F., Kind, R., Sondvol, E. & Zhao, W., 1999. Determination of the crustal structure in southern Tibet by dispersion and amplitude analysis of Rayleigh waves, *Geophys. J. Int.*, **138**, 809–819.
- Du, Z.J. *et al.*, 2002. Crustal structure beneath western and eastern Iceland from surface waves and receiver functions, *Geophys. J. Int.*, **149**, 349–363.
- Dueker, K.G. & A. Sheehan, F., 1998. Mantle discontinuity structure beneath the Colorado Rocky Mountains and High Plains, *J. geophys. Res.*, **103**, 7153–7169.
- Duret, F., Shapiro, N.M., Cao, Z., Levin, V., Molnar, P. & Roecker, S., 2010. Surface wave dispersion across Tibet: direct evidence for radial anisotropy in the crust, *Geophys. Res. Lett.*, **37**(16), L16306, doi:10.1029/2010GL043811.
- England, P. & Houseman, G., 1986. Finite strain calculations of continental deformation. Comparison with the India-Asia collision zone, *J. geophys. Res.*, **91**, 3664–3676.
- England, P. & Molnar, P., 1997. Active deformation of Asia: from kinematics to dynamics, *Science*, **278**, 647–650.
- Feng, M., An, M., Zhao, W., Xue, G., Mechie, J. & Zhao, Y., 2011. Lithosphere structures of northeast Tibetan Plateau and their geodynamic implications, *J. Geodyn.*, **52**(5), 432–442.
- Galvé, A. *et al.*, 2002. Modes of raising northeastern Tibet probed by explosion seismology, *Earth planet. Sci. Lett.*, **203**(1), 35–43.
- Guo, Z., Gao, X., Yao, H., Li, J. & Wang, W., 2009. Midcrustal low-velocity layer beneath the central Himalaya and southern Tibet revealed by ambient noise array tomography, *Geochem. Geophys. Geosyst.*, **10**(5), Q05007, doi:10.1029/2009GC002458.
- Guo, Z., Gao, X., Wang, W. & Yao, Z., 2012. Upper-and mid-crustal radial anisotropy beneath the central Himalaya and southern Tibet from seismic ambient noise tomography, *Geophys. J. Int.*, **189**(2), 1169–1182.
- Hacker, B.R., Ritzwoller, M.H. & Xie, J., 2014. Partially melted, mica-bearing crust in Central Tibet, *Tectonics*, **33**, 1408–1424.
- Huang, H., Yao, H. & van der Hilst, R.D., 2010. Radial anisotropy in the crust of SE Tibet and SW China from ambient noise interferometry, *Geophys. Res. Lett.*, **37**, L21310, doi:10.1029/2010GL044981.
- Jiang, C., Yang, Y. & Zheng, Y., 2014. Penetration of mid-crustal low velocity zone across the Kunlun Fault in the NE Tibetan Plateau revealed by ambient noise tomography, *Earth planet. Sci. Lett.*, **406**, 1–92.
- Jiang, M. *et al.*, 2006. Crustal thickening and variations in architecture from the Qaidam basin to the Qang Tang (North-Central Tibetan Plateau) from wide-angle reflection seismology, *Tectonophysics*, **412**(3), 121–140.
- Jiang, M., Zhou, S., Sandvol, E., Chen, X., Liang, X., John Chen, Y. & Fan, W., 2011. 3-D lithospheric structure beneath southern Tibet from Rayleigh-wave tomography with a 2-D seismic array, *Geophys. J. Int.*, **185**, 593–608.
- Jones, C.H. & Phinney, R.A., 1998. Seismic structure of the lithosphere from teleseismic converted arrivals observed at small arrays in the southern Sierra Nevada and vicinity, California, *J. geophys. Res.*, **103**(B5), 10065–10090.
- Julià, J., Ammon, C.J. & Herrmann, R.B., 2003. Lithospheric structure of the Arabian Shield from the joint inversion of receiver functions and surface wave group velocities, *Tectonophysics*, **371**, 1–21.
- Julià, J., Ammon, C.J. & Nyblade, A.A., 2005. Evidence for mafic lower crust in Tanzania, East Africa, from joint inversion of receiver functions and Rayleigh wave dispersion velocities, *Geophys. J. Int.*, **162**, 555–569.
- Julià, J., Ammon, C.J., Herrmann, R.B. & Correig, A.M., 2000. Joint inversion of receiver function and surface wave dispersion observations, *Geophys. J. Int.*, **143**, 99–112.
- Karplus, M.S., Zhao, W., Klemperer, S.L., Wu, Z., Mechie, J., Shi, D., Brown, L.D. & Chen, C., 2011. Injection of Tibetan crust beneath the south Qaidam Basin: evidence from INDEPTH IV wide-angle seismic data, *J. geophys. Res.*, **116**, B07301, doi:10.1029/2010JB007911.
- Karplus, M.S., Klemperer, S. L., Lawrence, J. F., Zhao, W., Mechie, J., Tilmann, F., Sandvol, E. & Ni, J., 2013. Ambient-noise tomography of north Tibet limits geological terrane signature to upper-middle crust, *Geophys. Res. Lett.*, **40**(5), 808–813.
- Kennett, B.L.N. & Engdahl, E.R., 1991. Traveltimes for global earthquake location and phase identification, *Geophys. J. Int.*, **105**(2), 429–465.
- Kind, R. *et al.*, 1996. Evidence from earthquake data for a partially molten crustal layer in southern Tibet, *Science*, **274**, 1692–1694.
- Kind, R. *et al.*, 2002. Seismic images of crust and upper mantle beneath Tibet: evidence for Eurasian plate subduction, *Science*, **298**, 1219–1221.
- Le Pape, F., Jones, A.G., Vozar, J. & Wenbo, W., 2012. Penetration of crustal melt beyond the Kunlun Fault into northern Tibet, *Nat. Geosci.*, **5**(5), 330–335.
- Ligorria, J.P. & Ammon, C.J., 1999. Iterative deconvolution and receiver-function estimation, *Bull. seism. Soc. Am.*, **89**, 1395–400.
- Li, Y., Wu, Q., Zhang, R., Tian, X. & Zeng, R., 2008. The crust and upper mantle structure beneath Yunnan from joint inversion of receiver functions and Rayleigh wave dispersion data, *Phys. Earth planet. Inter.*, **170**(1), 134–146.
- Li, H., Su, W., Wang, C.-Y. & Huang, Z., 2009. Ambient noise Rayleigh wave tomography in western Sichuan and eastern Tibet, *Earth planet. Sci. Lett.*, **282**, 201–211.
- Li, X., Wei, D., Yuan, X., Kind, R., Kumar, P. & Zhou, H., 2011. Details of the doublet Moho structure beneath Lhasa, Tibet, obtained by comparison of P and S receiver functions, *Bull. seism. Soc. Am.*, **101**, 1259–1269.
- Li, Y., Wu, Q., Pan, J., Zhang, F. & Yu, D., 2013a. An upper-mantle S-wave velocity model for East Asia from Rayleigh wave tomography, *Earth planet. Sci. Lett.*, **377**, 367–377.
- Li, L., Li, A., Shen, Y., Sandvol, E.A., Shi, D., Li, H. & Li, X., 2013b. Shear wave structure in the northeastern Tibetan Plateau from Rayleigh wave tomography, *J. Geophys. Res.: Solid Earth*, **118**(8), 4170–4183.
- Lin, F., Moschetti, M.P. & Ritzwoller, M.H., 2008. Surface wave tomography of the western United States from ambient seismic noise: Rayleigh and Love wave phase velocity maps, *Geophys. J. Int.*, **173**, 281–298.
- Lin, F.-C., Ritzwoller, M.H. & Snieder, R., 2009. Eikonal Tomography: surface wave tomography by phase-front tracking across a regional broad-band seismic array, *Geophys. J. Int.*, **177**(3), 1091–1110.
- Liu, F.T., Xu, P.F., Liu, J.S., Yin, Z.X., Qin, J.Y., Zhang, X.K., Zhang, C.K. & Zhao, J.R., 2003. The crustal velocity structure of the continental deep subduction belt: study on the eastern Dabie orogen by seismic wide-angle reflection/refraction, *Chin. J. Geophys.*, **46**(3), 366–372 (in Chinese with English abstract).
- Liu, M., Mooney, W.D., Li, S., Okaya, N. & Detweiler, S., 2006. Crustal structure of the northeastern margin of the Tibetan plateau from the

- Songpan–Ganzi terrane to the Ordos basin, *Tectonophysics*, **420**(1), 253–266.
- Luo, Y., Xu, Y. & Yang, Y., 2012. Crustal structure beneath the Dabie orogenic belt from ambient noise tomography, *Earth planet. Sci. Lett.*, **313–314**, 12–22.
- Mechie, J. *et al.*, 2012. Crustal shear (S) velocity and Poisson's ratio structure along the INDEPTH IV profile in northeast Tibet as derived from wide-angle seismic data, *Geophys. J. Int.*, **191**, 369–384.
- Metivier, F., Gaudemer, Y., Tapponnier, P. & Meyer, B., 1998. Northeastward growth of the Tibet Plateau deduced from balanced reconstruction of two depositional areas: the Qaidam and Hexi Corridor basins, *China Tectonics*, **17**, 823–842.
- Meyer, B., Tapponnier, P., Bourjot, L., Metivier, F., Gaudemer, Y., Peltzer, G., Guo, S. & Chen, Z., 1998. Crustal thickening in Gansu-Qinghai, lithospheric mantle subduction, and oblique, strike-slip controlled growth of the Tibet Plateau, *Geophys. J. Int.*, **135**, 1–47.
- Molnar, P., England, P. & Martinod, J., 1993. Mantle dynamics, uplift of the Tibetan plateau, and the Indian monsoon, *Rev. Geophys.*, **31**(4), 357–396.
- Nabelek, J. *et al.*, 2009. Underplating in the Himalaya-Tibet collision zone revealed by the Hi-CLIMB experiment, *Science*, **325**, 1371–1374.
- Niu, F. & Li, J., 2011. Component azimuths of the CEArray stations estimated from P-wave particle motion, *Earthq. Sci.*, **24**(1), 3–13.
- Ozalaybey, S., Savage, M.K., Sheehan, A.F., Louie, J.N. & Brune, J.N., 1997. Shear-wave velocity structure in the northern Basin and Range province from the combined analysis of receiver functions and surface waves, *Bull. seism. Soc. Am.*, **87**, 183–199.
- Pares, J.M., Van der Voo, R., Downs, W.R., Yan, M. & Fang, X.M., 2003. Northeastward growth and uplift of the Tibetan Plateau: Magnetostratigraphic insights from the Guide Basin, *J. geophys. Res.*, **108**(B1), 2017. doi:10.1029/2001JB001349.
- Pavlis, N.K., Holmes, S.A., Kenyon, S.C. & Factor, J.K., 2012. The development and evaluation of the Earth Gravitational Model 2008 (EGM2008), *J. geophys. Res.*, **117**, B04406, doi:10.1029/2011JB008916.
- Rapine, R., Tilmann, F., West, M., Ni, J. & Rodgers, A., 2003. Crustal structure of northern and southern Tibet from surface wave dispersion analysis, *J. geophys. Res.*, **108**(B2), doi:10.1029/2001JB000445.
- Ritzwoller, M.H., Lin, F.C. & Shen, W., 2011. Ambient noise tomography with a large seismic array, *C. R. Geosci.*, **343**, 558–570.
- Schulte-Pelkum, V., Monsalve, G., Sheehan, A.F., Pandey, M., Sapkota, S., Bilham, R. & Wu, F., 2005. Imaging the Indian subcontinent beneath the Himalaya, *Nature*, **435**, 1222–1225.
- Searle, M.P., Elliott, J.R., Phillips, R.J. & Chung, S.-L., 2011. Crustal-lithosphere structure and continental extrusion of Tibet, *J. geol. Soc. Lond.*, **168**, 633–672.
- Shapiro, N. & Ritzwoller, M., 2002. Monte-Carlo inversion for a global shear-velocity model of the crust and upper mantle, *Geophys. J. Int.*, **151**(1), 88–105.
- Shapiro, N.M., Ritzwoller, M.H., Molnar, P. & Levin, V., 2004. Thinning and flow of Tibetan crust constrained by seismic anisotropy, *Science*, **305**, 233–236.
- Shen, W., Ritzwoller, M.H., Schulte-Pelkum, V. & Lin, F.-C., 2013a. Joint inversion of surface wave dispersion and receiver functions: a Bayesian Monte-Carlo approach, *Geophys. J. Int.*, **192**(2), 807–836.
- Shen, W., Ritzwoller, M.H. & Schulte-Pelkum, V., 2013b. A 3-D model of the crust and uppermost mantle beneath the Central and Western US by joint inversion of receiver functions and surface wave dispersion, *J. geophys. Res.*, **118**(1), 262–276.
- Shen, W., Ritzwoller, M.H. & Schulte-Pelkum, V., 2013c. Crustal and uppermost mantle structure in the central U.S. encompassing the Midcontinent Rift, *J. geophys. Res.*, **118**, 4325–4344.
- Shi, D., Shen, Y., Zhao, W. & Li, A., 2009. Seismic evidence for a Moho offset and south-directed thrust at the easternmost Qaidam–Kunlun boundary in the Northeast Tibetan Plateau, *Earth planet. Sci. Lett.*, **288**(1), 329–334.
- Song, S.G., 1996. Metamorphic evolution of the coesite-bearing ultrahigh-pressure terrane in the North Qaidam, Northern Tibet, NWChina, *J. Metamorph. Geol.*, **21**(6), 631–644.
- Song, S., Zhang, L., Niu, Y., Su, L., Song, B. & Liu, D., 2006. Evolution from oceanic subduction to continental collision: a case study from the Northern Tibetan Plateau based on geochemical and geochronological data, *J. Petrol.*, **47**(3), 435–455.
- Song, S.G., Yang, J.S., Zhang, L.F., Wei, C.J. & Su, X.L., 2009. Metamorphic evolution of low-T eclogite from the North Qilian orogen, NW China: evidence from petrology and calculated phase equilibria in the system NCKFMASHO, *J. Metamorph. Geol.*, **27**(1), 55–70.
- Sun, Y., Niu, F., Liu, H., Chen, Y. & Liu, J., 2012. Crustal structure and deformation of the SE Tibetan plateau revealed by receiver function data, *Earth planet. Sci. Lett.*, **349**, 186–197.
- Sun, X. *et al.*, 2014. Crustal structure beneath SE Tibet from joint analysis of receiver functions and Rayleigh wave dispersion, *Geophys. Res. Lett.*, **41**(5), 1479–1484.
- Tapponnier, P., Zhiqin, X., Roger, F., Meyer, B., Arnaud, N., Wittlinger, G. & Jingsui, Y., 2001. Oblique stepwise rise and growth of the Tibet plateau, *Science*, **294**, 1671–1677.
- Tian, X. & Zhang, Z., 2013. Bulk crustal properties in NE Tibet and their implications for deformation model, *Gondwana Res.*, **24**(2), 548–559.
- Tian, X., Liu, Z., Si, S. & Zhang, Z., 2014. The crustal thickness of NE Tibet and its implication for crustal shortening, *Tectonophysics*, **634**, 198–207.
- Vergne, J., Wittlinger, G., Hui, Q., Tapponnier, P., Poupinet, G., Mei, J., Herquel, G. & Paul, A., 2002. Seismic evidence for stepwise thickening of the crust across the NE Tibetan plateau, *Earth planet. Sci. Lett.*, **203**(1), 25–33.
- Villasenor, A., Ritzwoller, M.H., Levshin, A.L., Barmin, M.P., Engdahl, E.R., Spakman, W. & Trampert, J., 2001. Shear velocity structure of Central Eurasia from inversion of surface wave velocities, *Phys. Earth planet. Inter.*, **123**(2–4), 169–184.
- Wang, Y.X. & Chen, J., 1987. *Metamorphic Zones and Metamorphism in Qinghai Province and Its Adjacent Areas*. Geological Publishing House, Beijing, pp. 213–220 (in Chinese with English abstract).
- Wang, C., Gao, R., Yin, A., Wang, H., Zhang, Y., Guo, T., Li, Q. & Li, Y., 2011. A mid-crustal strain-transfer model for continental deformation: A new perspective from high-resolution deep seismic-reflection profiling across NE Tibet, *Earth planet. Sci. Lett.*, **306**(3–4), 279–288.
- Wang, Y., Mooney, W.D., Yuan, X. & Okaya, N., 2013. Crustal structure of the northeastern Tibetan plateau from the southern Tarim Basin to the Sichuan Basin, *China Tectonophysics*, **584**(0), 191–208.
- Wang, W., Wu, J., Fang, L., Lai, G., Yang, T. & Cai, Y., 2014. S wave velocity structure in southwest China from surface wave tomography and receiver functions, *J. geophys. Res.*, **119**(2), 1061–1078.
- Wittlinger, G. *et al.*, 2004. Teleseismic imaging of subducting lithosphere and Moho offsets beneath western Tibet, *Earth planet. Sci. Lett.*, **221**(1), 117–130.
- Xie, J., Ritzwoller, M.H., Shen, W., Yang, Y., Zheng, Y. & Zhou, L., 2013. Crustal radial anisotropy across Eastern Tibet and the Western Yangtze Craton, *J. geophys. Res.*, **118**(8), 4226–4252.
- Xu, L., Rondenay, S. & van der Hilst, R.D., 2007. Structure of the crust beneath the southeastern Tibetan Plateau from teleseismic receiver functions, *Phys. Earth planet. Inter.*, **165**, 176–193.
- Xu, Q., Zhao, J., Pei, S. & Liu, H., 2013a. Distinct lateral contrast of the crustal and upper mantle structure beneath northeast Tibetan plateau from receiver function analysis, *Phys. Earth planet. Inter.*, **217**, 1–9.
- Xu, Z.J., Song, X. & Zhu, L., 2013b. Crustal and uppermost mantle S velocity structure under Hi-CLIMB seismic array in central Tibetan Plateau from joint inversion of surface wave dispersion and receiver function data, *Tectonophysics*, **584**, 209–220.
- Xu, T., Wu, Z., Zhang, Z., Tian, X., Deng, Y., Wu, C. & Teng, J., 2014. Crustal structure across the Kunlun fault from passive source seismic profiling in East Tibet, *Tectonophysics*, **627**, 98–107.
- Yang, J.J., Zhu, H., Deng, J.F., Zhou, T.Z. & Lai, S.C., 1994. Discovery of garnet-peridotite at the northern margin of the Qaidam basin and its significance, *Acta Petrol. Mineral.*, **13**, 97–105.
- Yang, J., Xu, Z., Zhang, J., Chu, C.-Y., Zhang, R. & Liou, J.-G., 2001. Tectonic significance of early Paleozoic high-pressure rocks in Altun-Qaidam-Qilian Mountains, northwest China, *Geological Soc. Am. Mem.*, **194**, 151–170.

- Yang, J.S., Xu, Z.Q., Zhang, J.X., Song, S.G., Wu, C.C.L., Shi, R.D., Li, H.B. & Brunel, M., 2002. Early Palaeozoic North Qaidam UHP metamorphic belt on the north-eastern Tibetan plateau and a paired subduction model, *TerraNova*, **14**(5), 397–404.
- Yang, Y. *et al.*, 2010. Rayleigh wave phase velocity maps of Tibet and the surrounding regions from ambient seismic noise tomography, *Geochem. Geophys. Geosyst.*, **11**(8), Q08010, doi:10.1029/2010GC003119.
- Yang, Y., Ritzwoller, M.H., Zheng, Y., Shen, W., Levshin, A.L. & Xie, Z., 2012. A synoptic view of the distribution and connectivity of the mid-crustal low velocity zone beneath Tibet, *J. geophys. Res.*, **117**(B4), B04303, doi:10.1029/2011JB008810.
- Yao, H., van Der Hilst, R.D. & Maarten, V., 2006. Surface-wave array tomography in SE Tibet from ambient seismic noise and two-station analysis—I. Phase velocity maps, *Geophys. J. Int.*, **166**(2), 732–744.
- Yao, H., Beghein, C. & van der Hilst, R.D., 2008. Surface wave array tomography in SE Tibet from ambient seismic noise and two-station analysis: II. Crustal and upper-mantle structure, *Geophys. J. Int.*, **163**, 205–219.
- Yao, H., van der Hilst, R.D. & Montagner, J.-P., 2010. Heterogeneity and anisotropy of the lithosphere of SE Tibet from surface wave array tomography, *J. geophys. Res.*, **115**, B12307, doi:10.1029/2009JB007142.
- Yin, A., Manning, C.E., Lovera, O., Menold, C.A., Chen, X. & Gehrels, G.E., 2007. Early paleozoic tectonic and thermomechanical evolution of ultrahigh-pressure (UHP) metamorphic rocks in the northern tibetan plateau, northwest China, *Int. Geol. Rev.*, **49**(8), 681–716.
- Yue, H. *et al.*, 2012. Lithospheric and upper mantle structure of the northeastern Tibetan Plateau, *J. geophys. Res.*, **117**, B05307, doi:10.1029/2011JB008545.
- Zhang, X.K. *et al.*, 2008. Crustal structures beneath West Qinling–East Kunlun orogen and its adjacent area—results of wide-angle seismic reflection and refraction experiment, *Chin. J. Geophys.*, **51**(2), 439–450 (in Chinese with English abstract).
- Zhang, J., Meng, F., Li, J. & Mattinson, C., 2009. Coesite in eclogite from the North Qaidam Mountains and its implications, *Chin. Sci. Bull.*, **54**(6), 1105–1110.
- Zhang, Z., Klemperer, S., Bai, Z., Chen, Y. & Teng, J., 2011a. Crustal structure of the Paleozoic Kunlun orogeny from an active-source seismic profile between Moba and Guide in East Tibet, China, *Gondwana Res.*, **19**(4), 994–1007.
- Zhang, Z., Deng, Y., Teng, J., Wang, C., Gao, R., Chen, Y. & Fan, W., 2011b. An overview of the crustal structure of the Tibetan plateau after 35 years of deep seismic sounding, *J. Asian Earth Sci.*, **40**, 977–989.
- Zhang, Z., Bai, Z., Klemperer, S., Tian, X., Xu, T., Chen, Y. & Teng, J., 2013. Crustal structure across northeastern Tibet from wide-angle seismic profiling: constraints on the Caledonian Qilian orogeny and its reactivation, *Tectonophysics*, **606**, 140–159.
- Zhang, X., Teng, J., Sun, R., Romanelli, F., Zhang, Z. & Panza, G.F., 2014. Structural model of the lithosphere–asthenosphere system beneath the Qinghai–Tibet Plateau and its adjacent areas, *Tectonophysics*, **634**, 208–226.
- Zhao, W. *et al.*, 2011. Tibetan plate overriding the Asian plate in central and northern Tibet, *Nat. Geosci.*, **4**(12), 870–873.
- Zheng, S., Sun, X., Song, X., Yang, Y. & Ritzwoller, M.H., 2008. Surface wave tomography of China from ambient seismic noise correlation, *Geochem. Geophys. Geosyst.*, **9**, Q0502, doi:10.1029/2008GC001981.
- Zheng, Y., Yang, Y., Ritzwoller, M.H., Zheng, X., Xiong, X. & Li, Z., 2010. Crustal structure of the northeastern Tibetan plateau, the Ordos block and the Sichuan basin from ambient noise tomography, *Earthq. Sci.*, **23**(5), 465–476.
- Zheng, Y., Shen, W., Zhou, L., Yang, Y., Xie, Z. & Ritzwoller, M.H., 2011. Crust and uppermost mantle beneath the North China Craton, northeastern China, and the Sea of Japan from ambient noise tomography, *J. geophys. Res.*, **116**, B12312, doi:10.1029/2011JB008637.
- Zhou, L., Xie, J., Shen, W., Zheng, Y., Yang, Y., Shi, H. & Ritzwoller, M.H., 2012. The structure of the crust and uppermost mantle beneath South China from ambient noise and earthquake tomography, *Geophys. J. Int.*, **189**(3), 1565–1583.
- Zhu, L. & Helmberger, D.V., 1998. Moho offset across the northern margin of the Tibetan plateau, *Science*, **281**, 1170–1172.